

A Bistate  $t$ -expansion Study of  $U(1)_{2+1}$  Lattice Gauge Theory<sup>\*</sup>

COLIN J. MORNINGSTAR

*Stanford Linear Accelerator Center**Stanford University, Stanford, California 94309*

## ABSTRACT

The compact formulation of  $U(1)$  Hamiltonian lattice gauge theory in  $2 + 1$  dimensions is studied using the  $t$ -expansion. The ground state energy, average plaquette, specific heat, photon mass gap, and the ratio of the two lowest masses are investigated. Two contraction techniques are applied: a unistate scheme which uses only the strong-coupling vacuum for the trial state, and a bistate scheme which allows the introduction of variational parameters and arbitrarily large loops of electric flux in one of the trial states. The mass ratio obtained from the bistate contraction scheme exhibits precocious scaling. No evidence of a stable scalar glueball is found.

Submitted to *Physical Review D*

---

<sup>\*</sup> Work supported by the Department of Energy, contract DE-AC03-76SF00515 and by the Natural Sciences and Engineering Research Council of Canada.

# 1. Introduction

Compact  $U(1)$  gauge theory in  $2 + 1$  dimensions has been the subject of many theoretical and numerical studies since the introduction of lattice gauge theory by Wilson<sup>[1]</sup> in Euclidean space-time and the subsequent development of the Hamiltonian formulation of lattice gauge theory by Kogut and Susskind.<sup>[2]</sup> Polyakov's pioneering study,<sup>[3]</sup> followed by the investigations of Banks *et al.*,<sup>[4]</sup> Glimm and Jaffe,<sup>[5]</sup> and Drell *et al.*,<sup>[6]</sup> showed that the periodicity of the magnetic portion of the action causes the theory to have a single linearly-confining phase and a nonzero mass gap in the photon sector. Estimates of the mass gap and string tension as a function of the inverse coupling  $\beta$  were obtained by these authors. Göpfert and Mack<sup>[7]</sup> exactly determined the mass gap in the Villain (periodic Gaussian) approximation to the Wilson theory and gave a rigorous lower bound on the string tension. Estimates of the ground state energy, the mean plaquette, the mass gap, and the string tension using strong-coupling perturbation theory,<sup>[8-12]</sup> variational methods,<sup>[13-19]</sup> and a WKB method using a weak-coupling Villain approximation<sup>[20]</sup> later appeared in the literature. Evidence that the string tension in  $U(1)_{2+1}$  undergoes a roughening transition near  $\beta \approx 0.7$  beyond which the on-axis strong-coupling series cannot be analytically continued was presented by several authors.<sup>[8][9][21][22]</sup> However, the behavior of the mass gaps is believed to be analytic near the roughening point.<sup>[10][22]</sup>

The earliest numerical investigations of  $U(1)_{2+1}$  were performed by Bhanot and Creutz,<sup>[23]</sup> D'Hoker,<sup>[24]</sup> and Ambjorn *et al.*<sup>[25]</sup> and were standard Wilson loop studies using Euclidean Monte Carlo methods. Sterling and Greensite<sup>[26]</sup> performed a notable simulation for a system with external sources and directly measured the string tension from energy differences rather than from Wilson loops. Other numerical methods which have been applied to  $U(1)_{2+1}$  include the Projector Monte Carlo method,<sup>[27][28]</sup> the Ensemble Projector Monte Carlo method,<sup>[29]</sup> Green's-function Monte Carlo,<sup>[30]</sup> the Guided Random Walk algorithm,<sup>[31]</sup> and a Langevin technique.<sup>[32]</sup>

Although the qualitative features of compact  $U(1)_{2+1}$  lattice gauge theory are

now well understood, the numerical values of the string tension and mass gap in the weak coupling region remain poorly determined. Also, the mass gap in the vacuum sector has not yet been reliably computed.

In this paper, compact  $U(1)_{2+1}$  Hamiltonian lattice gauge theory (HLGT) is studied using the  $t$ -expansion of Horn and Weinstein.<sup>[33]</sup> This method has been previously used to obtain glueball mass estimates in quenched  $SU(2)$ <sup>[34–36]</sup> and  $SU(3)$ <sup>[37–41]</sup> HLGT in 3+1 dimensions, as well as to study scaling in periodic QED.<sup>[42]</sup> The  $t$ -expansion uses the operator  $e^{-Ht}$  to project trial states onto the low-lying eigenstates of a Hamiltonian  $H$ . Estimates of expectation values are obtained through a process of power series expansion and subsequent series analysis. Although the method is a nonperturbative computational scheme for general Hamiltonian systems, it is particularly well-suited to systems defined on a lattice. The  $t$ -expansion, which will also be referred to here as the projector expansion method (PEM), resembles the high-temperature series expansion in statistical mechanics.

After describing the  $t$ -expansion in Sec. 2 and  $U(1)_{2+1}$  HLGT in Sec. 3, expansions for the ground state energy and photon mass gap are determined in Sec. 4. An important feature of this study is the fact that two contraction techniques are employed: a unistate scheme which uses only the strong-coupling vacuum as the trial state, and a new bistate scheme which allows the introduction of variational parameters and arbitrarily large loops of electric flux in one of the trial states. D-Padé approximants are used in the analysis of the series, which is presented in Sec. 5. Also in this section, the vacuum energy expansions are manipulated in order to study the mean plaquette and the so-called specific heat, quantities which provide clues to the phase structure of the theory and the location of the cross-over region from strong to weak coupling. An important finding of this paper is the effectiveness of the bistate contraction scheme in determining the photon mass gap and the ratio of the two lowest masses in the weak-coupling domain. Precocious scaling is observed in the mass ratio. Results and conclusions are summarized in Sec. 6.

## 2. The $t$ -expansion

The  $t$ -expansion uses  $e^{-tH}$  to project any trial state,  $|\psi_0\rangle$ , onto the true ground state,  $|\Psi_0\rangle$ , of Hamiltonian  $H$  as the arbitrary parameter  $t$  becomes large, provided that  $\langle\psi_0|\Psi_0\rangle \neq 0$ . The vacuum expectation value of an observable  $O$  is calculated in this method using

$$\langle O \rangle = \langle \Psi_0 | O | \Psi_0 \rangle = \lim_{t \rightarrow \infty} O(t), \quad (2.1)$$

where the *PEM function*,  $O(t)$ , is defined by

$$O(t) = \frac{\langle \psi_0 | e^{-Ht/2} O e^{-Ht/2} | \psi_0 \rangle}{\langle \psi_0 | e^{-Ht} | \psi_0 \rangle}. \quad (2.2)$$

Instead of employing stochastic techniques to evaluate this matrix element, the projector expansion method proceeds by expanding  $O(t)$  as a power series in  $t$ . This expansion yields

$$O(t) = \sum_{n=0}^{\infty} \frac{(-t)^n}{n!} O_n^c, \quad (2.3)$$

where the coefficients  $O_m^c$  are termed *PEM moments* and are defined recursively by<sup>[33]</sup>

$$\begin{aligned} O_m^c &= O_m - \sum_{p=1}^m \binom{m}{p} \langle \psi_0 | H^p | \psi_0 \rangle O_{m-p}^c, \\ O_m &= \frac{1}{2^m} \sum_{p=0}^m \binom{m}{p} \langle \psi_0 | H^p O H^{m-p} | \psi_0 \rangle. \end{aligned} \quad (2.4)$$

The PEM function must then be reconstructed somehow from its Taylor series in order for the limit  $t \rightarrow \infty$  to be taken. An interesting feature of the  $t$ -expansion is the fact that it exploits the formidable power of analytic continuation to deduce long-range behavior from short-range behavior, rather than resorting to statistical sampling.

The bistate contraction scheme<sup>[33]</sup> takes advantage of the fact that the trial states on the left- and right-hand sides of Eq. (2.2) need not be the same. The large  $t$  limit of the function

$$O_{\chi\psi}(t) = \frac{\langle \chi_0 | e^{-Ht/2} O e^{-Ht/2} | \psi_0 \rangle}{\langle \chi_0 | e^{-Ht} | \psi_0 \rangle} \quad (2.5)$$

also yields  $\langle O \rangle$ . The coefficients of the Taylor series expansion of this function are found as before using Eqs. (2.3) and (2.4) except that all operators are now taken between  $\langle \chi_0 |$  and  $| \psi_0 \rangle$ .

### 3. $U(1)_{2+1}$ HLGT

In the compact formulation of  $U(1)$  Hamiltonian lattice gauge theory studied here, the gauge field degrees of freedom reside on the links between the sites of a square two-dimensional spatial lattice with spacing  $a$ . With each link  $l$  is associated a link variable  $U_l$  which is a lattice version of the parallel transport matrix between the adjacent sites connected by the link.  $U_l$  is an element of the Lie group associated with the gauge invariance of the theory and in  $U(1)$  is related to the gauge field  $A_l$  corresponding to the link  $l$  by

$$U_l = e^{iaeA_l} = e^{i\theta_l}, \quad (3.1)$$

where  $e$  is the coupling constant of the theory and  $\theta_l = aeA_l$  is known as a link phase angle. The sum of the phase angles of the four links of an elementary square (plaquette) in the lattice, defined with respect to the direction of circulation around the plaquette, is a gauge-invariant quantity called a plaquette phase angle,  $\phi_p$ . In other words,  $\phi_p = (\nabla \times \theta)_p$ . The plaquette phase angle is related to the magnetic field  $B_p$  by  $\phi_p = a^2 e B_p$ . The dimensionless conjugate momentum associated with  $A_l$  is  $E_l = (a/e) \partial A_l / \partial t$  and in the temporal gauge measures the electric flux along

link  $l$ . The (dimensionless) Hamiltonian of the theory is given in terms of these quantities by<sup>[43]</sup>

$$H = \frac{1}{2\beta} \sum_l E_l^2 + \beta \sum_p (1 - \cos \phi_p), \quad (3.2)$$

where  $\beta = 1/g^2$  and  $g^2 = e^2 a$ . Both  $\beta$  and  $g$  are dimensionless. An important feature of the above Hamiltonian is its local gauge invariance.

This theory is quantized in the temporal gauge by imposing the following canonical commutation relations:

$$\left[ \theta(\vec{n}, \hat{j}), E(\vec{m}, \hat{i}) \right] = i \left( \delta(\vec{m}, \vec{n}) \delta(\hat{i}, \hat{j}) - \delta(\vec{n} + a\hat{j}, \vec{m}) \delta(\hat{i}, -\hat{j}) \right), \quad (3.3)$$

where in the above, directed link  $l = (\vec{n}, \hat{i})$  is specified by its site of origin  $\vec{n}$  and its direction  $\hat{i} = \pm \hat{e}_x, \pm \hat{e}_y$ . These commutators take into account that  $\theta(\vec{n}, \hat{j}) = -\theta(\vec{n} + a\hat{j}, -\hat{j})$  and  $E(\vec{n}, \hat{j}) = -E(\vec{n} + a\hat{j}, -\hat{j})$ . Since  $A^0 = 0$  is not a complete gauge-fixing condition, the theory contains spurious degrees of freedom. The physical states are identified as those which satisfy Gauss's law:

$$(\nabla \cdot E)_{\vec{n}} |\psi_{\text{phys}}\rangle = \sum_{\hat{i}=\pm\hat{e}_x, \pm\hat{e}_y} E(\vec{n}, \hat{i}) |\psi_{\text{phys}}\rangle = 0, \quad (3.4)$$

or in other words, those states which are gauge invariant.

A convenient basis in which to calculate PEM moments is the set of eigenstates of the electric flux operator. Each state  $|\{n\}\rangle$  in this so-called  $E$ -representation is specified by a set of integers  $\{n\}$  corresponding one-to-one with the links of the lattice. The total space of states is a tensor product of individual link state spaces. In this basis, the operators  $E_l$  are diagonal and the link variables  $U_l$  and  $U_l^\dagger$  are stepping operators. The state annihilated by every  $E_l$  is called the strong-coupling vacuum and is the state in which  $n_l = 0$  for all  $l$ .

Another convenient set of states is defined in the plaquette-flux representation. Electric flux configurations  $\{n\}$  which satisfy

$$n_l = -(\nabla \times m)_l, \quad (3.5)$$

where  $\{m\}$  is an integer-valued field, automatically satisfy Gauss's law. The set of integers  $\{m\}$  corresponding one-to-one with the plaquettes of the lattice can be used to label states in this representation. Every state  $|\{m\}\rangle_p$  in this set is gauge invariant. In two-dimensions with free boundary conditions, Eq. (3.5) uniquely determines the  $m_p$  and the states  $|\{m\}\rangle_p$  are orthogonal and form a complete set.<sup>[44]</sup> Note that this set of states is overcomplete (and thus nonorthogonal) in three dimensions and in two dimensions if periodic boundary conditions are imposed.

The continuum limit of the  $U(1)_{2+1}$  lattice theory is taken by varying the coupling  $g$  as  $a \rightarrow 0$  in such a way that some physical quantity is held at a fixed value. If the mass gap is held fixed as  $a \rightarrow 0$ , then  $g \rightarrow 0$  and the continuum limit exists,<sup>[7]</sup> leading not to familiar Maxwell electrodynamics but to a theory of massive glueballs. The string tension in units of the physical mass squared goes to infinity in this limit. Ordinary free electrodynamics is recovered by holding the unrenormalized electric charge  $e^2 = g^2/a$  fixed as  $a \rightarrow 0$ . It is not presently known whether or not the massless continuum limit obtained by fixing the string tension as  $a \rightarrow 0$  exists.

## 4. Calculation of the Moments

### 4.1 THE FINITE CLUSTER METHOD

The combinatorial complexity of PEM moment calculations in infinite lattice systems necessitates the use of an efficient and systematic computational approach. A procedure which is simple to implement and which provides ways of detecting errors is highly desirable, especially when calculating in the bistate contraction scheme. A method which readily satisfies these requirements is the finite cluster

method (FCM). This method was first put forward by Domb<sup>[45]</sup> in the application of the Mayer cluster integral theory to the Ising model. A formal proof of the method for the Ising and Heisenberg models was given by Rushbrooke<sup>[46]</sup> in 1964. The method was later generalized by Sykes *et al.*<sup>[47]</sup> who showed using only lattice constant theory that the method could be applied in the calculation of any quantity, regardless of the type of interaction, as long as that quantity is extensive in nature.

The finite cluster method relies heavily on graph theory. A *graph*  $G$  is a collection of vertices and bonds connecting the vertices. Any two vertices in a graph may be connected by at most one bond, and bonds which connect a vertex to itself are not permitted. Since the calculations in  $U(1)_{2+1}$  HLGIT performed here use the gauge-invariant plaquette-flux basis, the plaquettes are represented by graph vertices and the bonds represent the interplaquette electric mixings. A graph is termed *connected* if it contains at least one path of bonds between any two given vertices. A graph  $H$  is a *subgraph* of  $G$  if all of its vertices and bonds correspond to vertices and bonds of  $G$ . If  $S$  is a subset of the vertices in  $G$ , then a subgraph of  $G$  consisting of the vertices in  $S$  and *all* the bonds in  $G$  which connect the vertices in  $S$  is called a *section* graph. Any subgraph  $F'$  of a graph  $G$  which is isomorphic with a graph  $F$  represents an *embedding* of  $F$  in  $G$  in the *weak* sense. Any section graph  $\tilde{F}$  of  $G$  which is isomorphic with a graph  $F$  is an embedding of  $F$  in  $G$  in the *strong* sense. Clearly, a strong embedding is also a weak embedding, but the converse is not necessarily true. The number of distinct weak embeddings of  $G_1$  in  $G_2$  is denoted by  $(G_1; G_2)$  and is called the weak embedding constant of  $G_1$  in  $G_2$ ; the strong embedding constant of  $G_1$  in  $G_2$  is denoted by  $[G_1; G_2]$ . For example,  $[G_4; G_6] = 0$  and  $(G_4; G_6) = 4$ , referring to the graphs of Fig. 1. On a square two-dimensional lattice  $\mathcal{L}_{sq}$ ,  $[G_4; \mathcal{L}_{sq}] = 14$  (defined per site) and  $(G_4; \mathcal{L}_{sq}) = 18$ ; the embeddings of  $G_4$  in  $\mathcal{L}_{sq}$  in which the end vertices occupy nearest-neighbor sites of the lattice are allowed only as weak embeddings.

The usefulness of the FCM depends greatly on the property of *extensivity*. A quantity is extensive if, when evaluated on a disconnected graph, it is the sum of that quantity evaluated separately on the connected components of the graph. An

extensive matrix element  $A(\mathcal{L})$  defined on a regular lattice  $\mathcal{L}$  of infinite extent is calculated in the FCM by summing specific contributions, called the FCM weights, to  $A(\mathcal{L})$  from all connected finite-sized graphs  $G$  which can be embedded in  $\mathcal{L}$ . The procedure is prescribed by writing

$$A(\mathcal{L}) = \sum_{G \subseteq \mathcal{L}}^{(c)} [G; \mathcal{L}] \phi_A(G), \quad (4.1)$$

and similarly for all subgraphs,

$$A(G) = \sum_{F \subseteq G}^{(c)} [F; G] \phi_A(F), \quad (4.2)$$

where  $\phi_A(G)$  is the strong FCM weight for  $A$  on  $G$  and the (c) above the summation signs indicates that these sums include only connected subgraphs since  $A$  is extensive. By rewriting Eq. (4.2) in the following form:

$$\phi_A(G) = A(G) - \sum_{F \subset G}^{(c)} [F; G] \phi_A(F), \quad (4.3)$$

the FCM weights may be evaluated recursively using Eq. (4.3) on the connected subgraphs of  $\mathcal{L}$  in order of increasing size. Although these equations have been written in terms of strong embedding constants, weak embedding constants may also be used. When using strong constants, the size of a given graph  $G$  is the number of vertices in  $G$ ; for weak constants, the size of  $G$  is the total number of vertices and bonds in  $G$ .

## 4.2 GROUND STATE ENERGY DENSITY

Although the vacuum energy per plaquette is neither an interesting nor physically relevant quantity, its evaluation is important for three reasons: it is the simplest quantity which can be calculated and so provides a first test of the reliability of any computational algorithm; any nonanalyticity in this energy with respect to the inverse coupling  $\beta$  signals a phase transition; and interesting quantities, such as the mean plaquette, specific heat, and mass gaps, are obtained from manipulations of the ground state energy PEM function.

The PEM function  $\epsilon_0(t)$  for the ground state energy per plaquette is most easily calculated if each trial state is a tensor product of identical plaquette or link states. If one trial state,  $|\psi_0\rangle$ , lies entirely in the physical vacuum sector of Hilbert space, then the other,  $\langle\chi_0|$ , need not since the Hamiltonian in the projector does not mix states in different sectors. This aspect of the bistate contraction scheme is particularly important in nonabelian lattice gauge theories (which one ultimately wishes to study) where the strong-coupling vacuum is the only gauge-invariant state which is also a tensor product of individual link states. In such theories, this scheme allows the introduction of variational parameters and arbitrarily large loops of chromoelectric flux without sacrificing the simplicity of calculation afforded by the use of tensor product states.

Two PEM functions for the vacuum energy per plaquette are studied here. The first,  $\epsilon_0^A(t)$ , is given by

$$\epsilon_0^A(t) = \frac{\langle\varphi_0|\hat{H}e^{-2\beta Ht}|\varphi_0\rangle}{\langle\varphi_0|e^{-2\beta Ht}|\varphi_0\rangle},$$

where  $\hat{H}$  is the Hamiltonian per plaquette and  $|\varphi_0\rangle$  is the strong-coupling vacuum. The second function,  $\epsilon_0^B(t)$ , was chosen specifically to examine the effectiveness of the bistate contraction scheme and is given by

$$\epsilon_0^B(t) = \frac{\langle\varphi_0|\hat{H}e^{-2\beta Ht}|\varphi_{\lambda\omega}\rangle}{\langle\varphi_0|e^{-2\beta Ht}|\varphi_{\lambda\omega}\rangle},$$

where  $|\varphi_{\lambda\omega}\rangle$  is one of the simplest tensor-product states which can be formed,

$$|\varphi_{\lambda\omega}\rangle = \prod_p (1 + \lambda \cos \phi_p + i\omega \sin \phi_p) |\varphi_0\rangle, \quad (4.4)$$

with  $p$  labelling plaquettes. This state was chosen since it contains arbitrarily large loops of electric flux, yet is simple enough to permit the evaluation of at least the first ten or so terms in the  $t$ -expansion of the vacuum energy and the photon mass gap. In order to obtain reasonable estimates of continuum limit mass ratios, the effects of long-range correlations must be accurately deduced by the approximate means of analytic continuation used in the series analysis. This can only be accomplished if a sufficient number of terms in the  $t$ -expansion are known. In other words, one must not sacrifice too many terms in the expansion in order to improve the independent-plaquette trial state. Note also this state cannot be obtained from the action of any finite power of the Hamiltonian on the strong-coupling vacuum.

The calculation of a PEM moment  $H_n^c$  in any ground state energy expansion is accomplished in the following sequence of steps. First,  $H_n^c(G_1)$  on the smallest connected graph  $G_1$  is calculated. This is done by setting up an appropriate basis of states for the graph and constructing the Hamiltonian matrix  $H(G_1)$  and the trial state  $|\psi_0(G_1)\rangle$ , as well as  $|\chi_0(G_1)\rangle$  when using the bistate contraction scheme, in terms of these basis states.  $H_n^c(G_1)$  is then calculated using Eq. (2.4) with  $O = H$  and simple matrix multiplication. The FCM strong (or weak) weight  $\phi_{H_n^c}(G_1)$  is then determined using Eq. (4.3). Next, the above process is repeated for the second smallest connected graph  $G_2$  and then for successively larger connected graphs. On a given graph  $G$ ,  $\phi_{H_n^c}(G)$  can be nonzero only if  $n$  is sufficiently large to permit mixings among *all* of the plaquettes of  $G$ . Thus, for a given  $n$ , a graph  $G_c$  is eventually reached for which the FCM weight is zero; the weights for all larger graphs also vanish. If one is able to calculate the weights for all graphs smaller than  $G_c$ , then  $H_n^c$  on the infinite lattice can be determined using Eq. (4.1).

These calculations are performed using the symbolic manipulation package MAPLE. The use of such a language is crucial since it allows one to manipulate symbols, such as the coupling constant and variational parameters, and to treat numbers exactly, eliminating both round-off and overflow problems. The removal of overflow difficulties is very important because the combinatorics encountered in PEM lattice calculations can lead to very large numbers. The absence of round-off errors eliminates the problems which occur whenever differences between large nearly-equal numbers are taken.

The dimension of the basis of states required to evaluate PEM moments using the finite cluster method increases rapidly with the order of the moments. When calculating higher-order terms, one must consider not only larger connected diagrams, but also a larger number of states on the individual plaquettes. This growth in basis size limits the number of calculable terms in an expansion. However, many of the basis states needed to naively compute an FCM weight on a large graph participate only in contributions to the weight which are subsequently cancelled by subgraph subtractions. This fact can be exploited in order to significantly increase the number of PEM coefficients which can be determined. The easiest way to eliminate the unnecessary basis states is to impose a maximum plaquette flux magnitude. This maximum flux magnitude should be chosen as small as possible to minimize basis size, yet large enough in order to exactly compute the required weights. An FCM weight on a large graph can be computed using this basis truncation scheme only if all subgraph weights subtracted from it are calculated using the same truncation scheme.

The first *nineteen* coefficients in the power series expansion of  $\epsilon_0^A(t)$  and the first *twelve* in  $\epsilon_0^B(t)$  were obtained. The first several terms in these series are given below:

$$\epsilon_0^{A(B)}(t) = \sum_{n=0}^{\infty} \frac{(-t)^n}{n!} \epsilon_n^{A(B)}, \quad (4.5)$$

where

$$\begin{aligned}
\varepsilon_0^A &= \beta, \\
\varepsilon_1^A &= \beta^3, \\
\varepsilon_2^A &= 4\beta^3, \\
\varepsilon_3^A &= 16\beta^3 - 3\beta^7, \\
\varepsilon_4^A &= 64\beta^3 - 40\beta^7, \\
\varepsilon_5^A &= 40\beta^{11} - 208\beta^7 + 256\beta^3, \\
\varepsilon_6^A &= 1120\beta^{11} + 2560\beta^7 + 1024\beta^3, \\
\varepsilon_7^A &= 12544\beta^{11} - 1155\beta^{15} + 97792\beta^7 + 4096\beta^3, \\
\varepsilon_8^A &= -55440\beta^{15} - 46080\beta^{11} + 1996800\beta^7 + 16384\beta^3, \\
\varepsilon_9^A &= 57456\beta^{19} - 1071840\beta^{15} - 3071488\beta^{11} + 34317312\beta^7 + 65536\beta^3, \quad (4.6)
\end{aligned}$$

and

$$\begin{aligned}
\varepsilon_0^B &= (1 - \lambda/2)\beta, \\
\varepsilon_1^B &= (1 - \lambda^2/2)\beta^3 - 2\lambda\beta, \\
\varepsilon_2^B &= (3\lambda/2 - \lambda^3)\beta^5 + (-6\lambda^2 - 4\omega^2 + 4)\beta^3 - 8\lambda\beta, \\
\varepsilon_3^B &= (6\lambda^2 - 3\lambda^4 - 3)\beta^7 + (-24\lambda^3 - 32\lambda\omega^2 + 20\lambda)\beta^5 \\
&\quad + (-48\lambda^2 - 80\omega^2 + 16)\beta^3 - 32\lambda\beta, \\
\varepsilon_4^B &= (30\lambda^3 - 12\lambda^5 - 20\lambda)\beta^9 + (-120\lambda^4 - 240\lambda^2\omega^2 \\
&\quad + 160\lambda^2 + 80\omega^2 - 40)\beta^7 + (-320\lambda^3 - 1312\lambda\omega^2 + 104\lambda)\beta^5 \\
&\quad + (-256\lambda^2 - 1104\omega^2 + 64)\beta^3 - 128\lambda\beta, \\
\varepsilon_5^B &= (180\lambda^4 - 60\lambda^6 - 165\lambda^2 + 40)\beta^{11} + (-720\lambda^5 \\
&\quad - 1920\lambda^3\omega^2 + 1320\lambda^3 + 1440\lambda\omega^2 - 560\lambda)\beta^9 + (-2400\lambda^4 \\
&\quad - 16416\lambda^2\omega^2 - 1120\omega^4 + 1968\lambda^2 + 2912\omega^2 - 208)\beta^7 \\
&\quad + (-2112\lambda^3 - 33184\lambda\omega^2 - 1280\lambda)\beta^5 + (32\lambda^2 - 13120\omega^2 \\
&\quad + 256)\beta^3 - 512\lambda\beta. \quad (4.7)
\end{aligned}$$

The connected diagrams needed to compute these moments are shown in Fig. 1. In this figure, plaquettes are represented by circles, and the line segments connecting the circles represent the links on the lattice shared by adjacent plaquettes.

### 4.3 PHOTON MASS GAP

PEM functions for energy gaps are not extensive but can be obtained from functions which are. To calculate an energy gap in a sector ( $\alpha$ ) which does not contain the ground state, first evaluate the following extensive ratio:

$$R_{\Delta_1^\alpha}(t) = \frac{\langle \psi_1^\alpha | e^{-tH} | \psi_1^\alpha \rangle}{\langle \psi_0 | e^{-tH} | \psi_0 \rangle}, \quad (4.8)$$

where  $|\psi_1^\alpha\rangle = \Omega_\alpha |\psi_0\rangle$  and  $\Omega_\alpha$  is an operator with the following properties: if  $|\psi_0\rangle$  lies entirely in the vacuum sector of Hilbert space, then  $\Omega_\alpha |\psi_0\rangle$  lies entirely in the ( $\alpha$ ) sector;  $\Omega_\alpha$  is an extensive local operator, *i.e.*, it satisfies

$$\begin{aligned} \Omega_\alpha(\mathcal{G}_1 \cup \mathcal{G}_2) &= \Omega_\alpha(\mathcal{G}_1) + \Omega_\alpha(\mathcal{G}_2), \\ [\Omega_\alpha(\mathcal{G}_1), H(\mathcal{G}_2)] &= 0, \\ [\Omega_\alpha(\mathcal{G}_2), H(\mathcal{G}_1)] &= 0, \end{aligned} \quad (4.9)$$

where  $\mathcal{G}_1$  and  $\mathcal{G}_2$  denote the embeddings of connected graphs  $G_1$  and  $G_2$  in  $\mathcal{L}$  such that  $\mathcal{G}_1 \cap \mathcal{G}_2 = \emptyset$ .  $\Omega_\alpha$  is usually chosen to project out a state of definite momentum and angular momentum. The energy gap in the ( $\alpha$ ) sector is then obtained using

$$\Delta_1^{(\alpha)}(t) = - \frac{\partial}{\partial t} \ln R_{\Delta_1^\alpha}(t) \quad (4.10)$$

$$= \frac{\langle \psi_1^\alpha | H e^{-tH} | \psi_1^\alpha \rangle}{\langle \psi_1^\alpha | e^{-tH} | \psi_1^\alpha \rangle} - \frac{\langle \psi_0 | H e^{-tH} | \psi_0 \rangle}{\langle \psi_0 | e^{-tH} | \psi_0 \rangle}. \quad (4.11)$$

The ground state energy of a lattice system is proportional to  $N_s$ , the (infinite) number of sites in the lattice, whereas energy gaps are finite values, independent of  $N_s$  as  $N_s \rightarrow \infty$ . The second ratio in Eq. (4.11) tends to the ground state energy

as  $t \rightarrow \infty$  and thus, is proportional to  $N_s$ ; the first ratio is a sum of a function proportional to  $N_s$ , which tends to the ground state energy as  $t \rightarrow \infty$ , and a function independent of  $N_s$ , which tends to the energy gap as  $t$  becomes large. In choosing  $|\psi_1^\alpha\rangle$  as suggested above, the  $\mathcal{O}(N_s)$  terms *explicitly cancel for all values of  $t$*  in the difference of the ratios in Eq. (4.11). This explicit and exact nullification of vacuum noise in energy gap calculations is an attractive and important feature of the projector expansion method.

The bistate contraction scheme can also be used to formulate a non-vacuum sector energy gap expansion in which the  $\mathcal{O}(N_s)$  contributions explicitly cancel. If the tensor product state  $|\chi_0\rangle$  lies partially in the vacuum sector and partially in the  $(\alpha)$  sector, then the following extensive ratio,

$$R_{\Delta_1^\alpha}^b(t) = \frac{\langle \chi_0 | e^{-tH} | \psi_1^\alpha \rangle}{\langle \chi_0 | e^{-tH} | \psi_0 \rangle}, \quad (4.12)$$

yields the appropriate energy gap via Eq. (4.10). The coefficients in the Taylor series expansions of  $R_{\Delta_1^\alpha}(t)$  and  $R_{\Delta_1^\alpha}^b(t)$  are calculated in the same manner as the  $H_n^c$  moments. After the contributions to these coefficients from the connected subgraphs are summed as in Eq. (4.1), the energy gap moments are obtained from the logarithmic derivative using Eq. (4.10).

The photon mass gap is an important physical quantity. It is given by the difference between the energy of the vacuum and the energy of the lowest state which is antisymmetric under lattice reflections and invariant under all lattice translations and  $\pi/2$  rotations. The inverse of this mass gap yields the correlation length of the lattice theory in terms of the lattice spacing. The photon mass may also be used to renormalize the theory; all other physical quantities, when expressed in terms of this mass, tend naturally to their physical values as the continuum limit is taken.

Two PEM functions for the photon mass  $M$  are studied here. The first,  $M^A(t)$ ,

is defined by

$$M^A(t) = \frac{\langle \varphi_1 | H e^{-2\beta H t} | \varphi_1 \rangle}{\langle \varphi_1 | e^{-2\beta H t} | \varphi_1 \rangle} - \frac{\langle \varphi_0 | H e^{-2\beta H t} | \varphi_0 \rangle}{\langle \varphi_0 | e^{-2\beta H t} | \varphi_0 \rangle}, \quad (4.13)$$

where  $|\varphi_0\rangle$  is the strong-coupling vacuum and

$$|\varphi_1\rangle = \sum_p \sin \phi_p |\varphi_0\rangle \quad (4.14)$$

is a zero-momentum state in the photon sector. The second function,  $M^B(t)$ , is a bistate contraction given by

$$M^B(t) = \frac{\langle \varphi_1 | H e^{-2\beta H t} | \varphi_{\lambda\omega} \rangle}{\langle \varphi_1 | e^{-2\beta H t} | \varphi_{\lambda\omega} \rangle} - \frac{\langle \varphi_0 | H e^{-2\beta H t} | \varphi_{\lambda\omega} \rangle}{\langle \varphi_0 | e^{-2\beta H t} | \varphi_{\lambda\omega} \rangle}, \quad (4.15)$$

where  $|\varphi_{\lambda\omega}\rangle$  is the tensor product state defined in Eq. (4.4). The coefficients in the power series expansions of  $M^A(t)$  and  $M^B(t)$  were calculated using the finite cluster method and the basis truncation procedure described in the previous section. The first *fifteen* terms in  $M^A(t)$  and the first *eleven* terms in  $M^B(t)$  were computed. Several of these terms are listed below:

$$M^{A(B)}(t) = \sum_{n=0}^{\infty} \frac{(-t)^n}{n!} M_n^{A(B)}, \quad (4.16)$$

where

$$\begin{aligned} M_0^A &= 2/\beta, \\ M_1^A &= -\beta^3/2, \\ M_2^A &= -6\beta^3, \\ M_3^A &= 5\beta^7/2 + 8\beta^3, \\ M_4^A &= 100\beta^7 + 576\beta^3, \\ M_5^A &= 872\beta^7 - 75\beta^{11}/2 + 9152\beta^3, \end{aligned}$$

$$\begin{aligned}
M_6^A &= 992 \beta^7 - 3150 \beta^{11} + 119424 \beta^3, \\
M_7^A &= 1127 \beta^{15} - 68880 \beta^{11} + 150144 \beta^7 + 1472768 \beta^3, \\
M_8^A &= 162288 \beta^{15} - 813888 \beta^{11} + 15594496 \beta^7 + 17834496 \beta^3, \\
M_9^A &= 6332928 \beta^{15} - 56910 \beta^{19} - 10023680 \beta^{11} + 785082624 \beta^7 \\
&\quad + 214664192 \beta^3, \tag{4.17}
\end{aligned}$$

and

$$\begin{aligned}
M_0^B &= \lambda\beta/2 + 2/\beta, \\
M_1^B &= (\lambda^2 - 1)\beta^3/2 + 6\lambda\beta, \\
M_2^B &= (\lambda^3 - 3\lambda/2)\beta^5 + (18\lambda^2 + 8\omega^2 - 6)\beta^3 + 32\lambda\beta, \\
M_3^B &= (3\lambda^4 - 6\lambda^2 + 5/2)\beta^7 + (72\lambda^3 + 64\lambda\omega^2 - 60\lambda)\beta^5 \\
&\quad + (256\lambda^2 + 232\omega^2 + 8)\beta^3 + 144\lambda\beta, \\
M_4^B &= (12\lambda^5 - 30\lambda^3 + 20\lambda)\beta^9 + (360\lambda^4 + 480\lambda^2\omega^2 - 480\lambda^2 \\
&\quad - 160\omega^2 + 100)\beta^7 + (1920\lambda^3 + 4016\lambda\omega^2 - 584\lambda)\beta^5 \\
&\quad + (2720\lambda^2 + 3696\omega^2 + 576)\beta^3 + 608\lambda\beta, \\
M_5^B &= (60\lambda^6 - 180\lambda^4 + 165\lambda^2 - 75/2)\beta^{11} + (2160\lambda^5 \\
&\quad + 3840\lambda^3\omega^2 - 3960\lambda^3 - 2880\lambda\omega^2 + 1680\lambda)\beta^9 + (15360\lambda^4 \\
&\quad + 51408\lambda^2\omega^2 + 3200\omega^4 - 11568\lambda^2 - 9136\omega^2 + 872)\beta^7 \\
&\quad + (36624\lambda^3 + 127568\lambda\omega^2 + 2000\lambda)\beta^5 + (25056\lambda^2 + 45536\omega^2 \\
&\quad + 9152)\beta^3 + 2496\lambda\beta. \tag{4.18}
\end{aligned}$$

## 5. Series Analysis

D-Pad  approximants<sup>[33][34]</sup> are used in the analysis of the series studied here. Ideally, one would prefer to use more than one method of series analysis; however, no other method has yet been found which is sufficiently accurate to provide a useful check of the D-Pad  estimates. Instead, confidence in the PEM function reconstruction must stem from agreement among many of the  $[L/M]$  D-Pad  approximants and from adequate convergence in the approximants as  $L + M$  increases.

Series analysis results are presented here as the averages and standard deviations of selected approximants. High  $L + M$  approximants which occur in a cluster are typically chosen. The standard deviation in the values of the chosen approximants yields an estimate of the uncertainty in the extrapolation. It should be stressed that such "error" estimates are in no sense rigorous and represent only a subjective assessment of the rate of convergence of the available approximants.

In the bistate contraction scheme, the problem of choosing best values for the variational parameters in the trial states must be addressed. If many terms in the power series representation of a PEM function are known, then the values chosen should be immaterial. However, if only the first ten or so terms are available, one must expect that certain values of these parameters will yield better estimates than others. Note that the bistate PEM function for the ground state energy does not provide an upper bound on the true energy and that D-Pad  approximants are also not guaranteed to lie above the exact energy.

In the evaluation of the ground state energy and other vacuum expectation values, one expects that improvement in the starting states will lead to better convergence in the D-Pad  approximants and more reliable series analysis results. Hence, separate application of the variational principle to *each* trial state is a good starting point for the bistate series analysis. If adequate convergence of the approximants is observed using these variationally-optimal parameter values, and if the average of the selected approximants does not change appreciably under small variations in the parameters about these chosen values, then the bistate series

analysis is complete. However, if these conditions are not met, one of the simplest ways to proceed is to search parameter space for a region of good convergence by freely varying one of the parameters, determining all others by the variational method. Often, physical insight can be an important guide in this search.

## 5.1 THE GROUND STATE ENERGY PER PLAQUETTE

The results of the D-Padé analysis of  $\epsilon_0^A(t)$  and  $\epsilon_0^B(t)$  are presented in Table 1. The  $\epsilon_0^A$  estimates are averages of the following eighteen approximants: [2/8 – 11], [3/8 – 12], [4/9 – 13], [5/10 – 12], and [6/11]. The bistrate  $\epsilon_0^B$  averages include the following eight approximants: [1/6 – 9], [2/6 – 8], and [3/7], and values of  $\lambda$  and  $\omega$  which minimize the expectation value of the Hamiltonian in the state  $|\varphi_{\lambda\omega}\rangle$  are used; this minimum occurs at  $\omega = 0$  and for real values of  $\lambda$  as shown in Fig. 2. The series analysis results were insensitive to the values of  $\lambda$  and  $\omega$  in this region of parameter space. Agreement between the bistrate and unistate estimates is excellent. The results compare favorably to those of the guided random walk (GRW) algorithm on an  $8 \times 8$  lattice<sup>[31]</sup> (which are presently the best estimates of the  $U(1)_{2+1}$  HLG T vacuum energy density from any stochastic method) and agree well with strong- and weak-coupling perturbation theory. No evidence of a phase transition appears.

## 5.2 THE MEAN PLAQUETTE

The smoothness in the dependence of the average plaquette  $\langle \cos \phi_p \rangle$  on  $\beta$  in the cross-over region between strong and weak coupling is of interest here, since a discontinuity in this dependence indicates a phase transition. (For example, in (3+1)-dimensional  $U(1)$  HLG T, there is a second-order transition near  $\beta \approx 1$  from a confining massive phase in strong coupling to a massless Coulomb phase in weak coupling.)

Two PEM functions whose large  $t$  limits yield  $\langle \cos \phi_p \rangle$  are investigated here. The power series expansions  $\langle \cos \phi_p \rangle^A(t)$  and  $\langle \cos \phi_p \rangle^B(t)$  are obtained by manip-

ulating the ground state energy density series  $\epsilon_0^A(t)$  and  $\epsilon_0^B(t)$ , respectively, using the Feynman-Hellmann theorem:

$$\langle \cos \phi_p \rangle^\alpha(t) = 1 - \frac{\partial}{\partial \rho} [\beta \epsilon_0^\alpha(t)], \quad \alpha = A, B, \quad (5.1)$$

where  $\rho = \beta^2$  and the validity of the termwise differentiation with respect to  $\beta$  of the ground state energy PEM power series has been assumed.

The D-Padé estimates of the mean plaquette are given in Table 2. The averages in the first column include the following fourteen approximants:  $[3/8 - 12]$ ,  $[4/9 - 13]$ ,  $[5/10 - 12]$ , and  $[6/11]$ . The bistate averages in the second column include the following seven approximants:  $[1/6 - 7]$ ,  $[2/6 - 8]$ , and  $[3/6 - 7]$ . The variational parameter values used in these averages are the same as those used for the ground state energy density. Agreement of the unistate and bistate estimates with each other and with strong- and weak-coupling perturbation theory is excellent. The results again compare favorably to those of GRW, particularly for large  $\beta$ . There is no evidence of a phase transition.

### 5.3 THE SPECIFIC HEAT

In statistical mechanics, the specific heat is the second derivative of the free energy with respect to temperature,  $C_V = -T(\partial^2 F / \partial T^2)_V$ . The analogue of the free energy in Euclidean lattice gauge theory is the ground state energy<sup>[43]</sup>, and the coupling constant is the analogue of the temperature. Hence, the following quantity,

$$C(\beta) = -\frac{\partial^2}{\partial \beta^2} \epsilon_0(\beta), \quad (5.2)$$

is here referred to as the specific heat.

This quantity is interesting for two main reasons: first, discontinuities in  $C(\beta)$  with respect to  $\beta$  reveal phase transitions in the lattice theory; and secondly,  $C(\beta)$  peaks in the cross-over region between strong- and weak-coupling behavior<sup>[34]</sup>,

providing valuable information concerning the location in  $\beta$  at which the onset of continuum limit scaling may be expected.

The D-Padé estimates of the specific heat using only the series  $C^A(t)$  obtained from  $\epsilon_0^A(t)$  are shown in Fig. 3. These estimates are averages of the following fourteen approximants:  $[3/10 - 14]$ ,  $[4/10 - 13]$ ,  $[5/10 - 12]$ , and  $[6/10 - 11]$ . Again, there is no evidence of a phase transition. The specific heat peaks near  $\beta \approx 0.8$ , suggesting that weak-coupling behavior may set in for  $\beta$  near unity.

#### 5.4 THE PHOTON MASS

The weak-coupling behavior of the mass gap is not exactly known. Göpfert and Mack<sup>[7]</sup> showed that the lattice photon mass in the Villain (periodic Gaussian) action defined on a (2+1)-dimensional Euclidean lattice is given exactly by

$$M^2 = 8\pi^2\beta \exp[-2\pi^2\beta V(0)], \quad (5.3)$$

where  $V(0) \simeq 0.252731$  is the lattice Coulomb Green function at contact. In the Hamiltonian formalism in which only the spatial dimensions are discretized,  $V_H(0) \simeq 0.321441$  is the analogous Green function at contact. It is often claimed in the literature that the Villain action is a high- $\beta$  approximation of the Wilson action so that Eq. (5.3) should also give the mass gap in the weak-coupling limit of the Wilson formulation of the theory. However, Suranyi<sup>[20]</sup> has disputed this, asserting that a natural series of models, beginning with periodic Gaussian and approximating the Wilson model with arbitrary precision, does not exist. His argument is based on the fact that periodic Gaussian models are special forms of Wannier function expansions.

Several calculations have also provided evidence that the mass gap in the Wilson formulation of  $U(1)_{2+1}$  HLG T does not fall off in the weak-coupling region in the same manner as in the Villain model. Using a WKB variational method, Suranyi<sup>[20]</sup> deduced an exponential fall-off with a decay factor  $5.7 \pm 0.1$ . Heys and

Stump<sup>[19]</sup>, in a six parameter variational calculation, found

$$M^2 = (500 \pm 30)\beta \exp[-(4.97 \pm 0.05)\beta], \quad (5.4)$$

fitting their results for  $\beta > 1.2$  to the above form. Hamer and Irving<sup>[12]</sup>, using a strong-coupling linked-cluster expansion technique, deduced

$$M^2 = (470 \pm 200)\beta \exp[-(5.3 \pm 0.5)\beta], \quad (5.5)$$

again fitting their results to this form. These two results are consistent with each other but differ from the Villain prediction,  $M^2 = 78.96\beta \exp(-6.345\beta)$  (after converting the lattice Coulomb Green function from the Lagrangian to the Hamiltonian formalism), both in slope and overall magnitude.

The results of the D-Padé series analysis of  $M^A(t)$  and  $M^B(t)$  are shown in Fig. 4. The  $M^A$  estimates, indicated by circles, are averages of the following twelve approximants:  $[3/5 - 10]$ ,  $[4/6 - 9]$ , and  $[5/7 - 8]$ ; the  $M^B$  estimates, shown as squares, are averages of the  $[2/5 - 7]$  and  $[3/6]$  D-Padé approximants. In the bistate estimates  $M^B$ , the variationally-optimal values of  $\lambda$  and  $\omega$  calculated previously were used (note that although the projection of  $|\varphi_{\lambda\omega}\rangle$  onto the photon sector is proportional to  $\omega$ , the limit  $\omega \rightarrow 0$  can be used since this proportionality factor appears in both the numerator and denominator in the first ratio in Eq. (4.15)). The smallest spread in the selected approximants occurs in this region of parameter space. The results interpolate smoothly between strong-coupling behavior, shown by the dashed curve, and an exponential decay in the weak-coupling region. Agreement between the unistate and bistate estimates is excellent for  $\beta < 1.5$ . At this value of the inverse coupling, the spread in the  $M^A$  approximants begins to grow and their average starts to deviate from the exponential decay. The bistate estimates continue to exhibit the expected weak-coupling behavior until near  $\beta \approx 2$ . For larger  $\beta$ , more terms in the  $t$ -expansion are apparently necessary. A fit of the bistate estimates for  $1 \leq \beta \leq 2$  and the  $M^A$  estimates for  $1 \leq \beta \leq 1.4$  to the

form  $M^2 = a\beta \exp(-b\beta)$  yields the following weak-coupling mass gap behavior:

$$M^2 = (380 \pm 20)\beta \exp[-(5.23 \pm 0.04)\beta]. \quad (5.6)$$

This fit is shown in Fig. 4 by a solid line. The results of Hamer and Irving (the dotted line) and Heys and Stump (the dashed-dotted line) are also shown. Agreement with the results of Hamer and Irving is particularly remarkable.

### 5.5 THE MASS GAP IN THE VACUUM SECTOR

The quantity of interest here is the ratio of the mass gap in the vacuum sector  $M_g$  to the lattice photon mass  $M$  as  $\beta \rightarrow \infty$ . In this limit, the ratio  $R_g = M_g/M$  is expected to tend smoothly to its continuum limit value. In practice, this limiting value is found by increasing  $\beta$  from strong coupling until the mass ratio  $R_g(\beta)$  levels off in the weak-coupling region. From the previous studies of the photon mass and the specific heat, one would expect the scaling of  $R_g$  to set in for  $\beta > 1$ . If the continuum theory admits a stable bound state of two photons (a glueball), then the weak coupling limit of  $R_g$  will lie between unity and two. If the continuum theory is simply a free field theory of massive scalar photons, as in the Villain model<sup>[7]</sup>, or if the glueball remains in the continuum theory only as a resonance, then a ratio  $R_g = 2$  should be observed as  $\beta$  becomes large. Alessandrini *et al.*<sup>[10]</sup>, using strong-coupling perturbation theory, examined this ratio and tentatively concluded that a stable glueball in the vacuum sector did not exist in the continuum limit. Hamer and Irving<sup>[12]</sup> found  $R_g = 2.1 \pm 0.5$  in the weak-coupling limit. However, their estimate was based solely on a single Shafer extrapolation of the strong-coupling perturbation series.

Two power series for the ratio  $R_g$  are studied here. The first series,  $R^A(t)$ , is determined using<sup>[34]</sup>

$$R^A(t) = -\frac{1}{2\beta} \frac{\partial}{\partial t} \ln \left( -\frac{\partial}{\partial t} \epsilon_0^A(t) \right) / M^A(t). \quad (5.7)$$

The second series,  $R^B(t)$ , is obtained from the bistrate contraction and is given by

$$R^B(t) = -\frac{1}{2\beta} \frac{\partial}{\partial t} \ln \left( \frac{\partial}{\partial \lambda} \epsilon_0^B(t) \right) / M^B(t). \quad (5.8)$$

The results of the D-Padé series analysis of  $R^A(t)$  are shown as circles in Fig. 5. These estimates are averages of the following twelve D-Padé approximants:  $[1/7 - 12]$  and  $[2/6 - 11]$ . The  $L = 0$  approximants are not used since they do not reproduce the behavior of the Taylor series for all values of  $t$  lying in the range  $0 < t < t_m$ , where  $t_m$  is the largest value of  $t$  for which the truncated Taylor series exhibits sufficient convergence to be judged a reliable representation of the PEM function. These  $L = 0$  approximants decay much too quickly and agree with the Taylor series only for  $0 < t < t_0$ , where  $t_0 \ll t_m$ . In the strong-coupling region, most of the approximants agree very well with one another and with strong-coupling perturbation theory (the solid curve), but as  $\beta$  is increased, a sharp change in their behavior is observed. For  $\beta > 1.2$ , the approximants with  $L > 2$  suddenly begin climbing in value and disagree radically with one another. The  $R^A$  estimates exhibit slight evidence of scaling. They almost level off at an overly large value of  $R_g \approx 2.3$  near  $\beta \approx 2$  just before the spread in the selected approximants suddenly grows. The key observation here is that there is no evidence of a stable glueball in the continuum limit.

This conclusion is confirmed by the results of the analysis of the  $R^B(t)$  series. These bistrate estimates, indicated by squares in Fig. 5, are averages of the following thirteen approximants:  $[0/6 - 9]$ ,  $[1/5 - 8]$ ,  $[2/5 - 7]$  and  $[3/5 - 6]$ . In order to take advantage of any cancellations which might occur in  $R^B(t)$ , the same values of  $\lambda$  and  $\omega$  are used in both the numerator and denominator of Eq. (5.8). In the strong-coupling region, most of the approximants agree very well with one another. Parameter values near the variationally-optimal ones yield the least amount of spread in the selected approximants and averages which are insensitive to the values of  $\lambda$  and  $\omega$ . Thus, for  $\beta \leq 0.8$ , the variationally-optimal values of  $\lambda$  and

$\omega$  are used. Agreement between the bistate and unistate estimates is excellent in this region of the coupling.

As  $\beta$  is further increased, the variances in the bistate estimates obtained using the variationally-optimal parameter values begin to grow quickly, similar to the  $R^A$  estimates. However, a region of averages with much smaller variances suddenly appears for  $\omega^2 < 0$  and satisfying  $1 < |\omega| < 2$ . Hence, for  $\beta > 0.8$ , the bistate estimates are obtained in the following manner: first,  $\omega$  is varied, keeping  $\omega^2$  real (this ensures that all coefficients in  $R^B(t)$  are real, simplifying the series analysis since the requirement  $\lim_{t \rightarrow \infty} \Im R^B(t) = 0$  is automatically satisfied); for each value of  $\omega$ , the parameter  $\lambda$  is then chosen by minimizing the ground state energy in the state  $|\varphi_{\lambda\omega}\rangle$ ; the estimate with the smallest standard deviation is finally selected. This procedure is illustrated in Fig. 6. For  $\beta = 0.8$ , the minimum in the standard deviation of the selected D-Padé approximants occurs for  $\omega = 0$  (see Fig. 6(a)); for  $\beta = 1.3$ , best convergence of the approximants occurs for  $\omega \approx \pm 1.65i$  (see Fig. 6(b)). For various values of  $\beta$  in the region  $0.8 < \beta < 2.5$ , a large search of parameter space was undertaken and all other parameter values which were tried produced estimates which either were consistent with those obtained using the above procedure or had much larger variances.

The bistate estimates provide much stronger evidence of continuum limit scaling than do the  $R^A$  estimates. The ratio  $R_g$  determined from the bistate contraction becomes nearly constant for  $\beta > 2$  and seems to be approaching a slightly high value of 2.2, providing further evidence that no stable scalar glueball exists in this theory.

## 6. Conclusion

The ground state energy per plaquette, the average plaquette, and the specific heat in  $U(1)_{2+1}$  HLGT were accurately determined on an infinite lattice for a wide range of coupling constant values, confirming that this lattice theory has only a single confining phase. The results agreed very well with strong- and weak-coupling perturbation theory and compared favorably to results from stochastic Hamiltonian methods. Two trial states were used: the strong-coupling vacuum and a tensor product of single-plaquette states which were linear combinations of field configurations with zero or one unit of electric flux circulating along the plaquette boundary. A single-state and a bistate contraction were calculated. Although the bistate estimates for the ground state energy and mean plaquette were no better than those determined using only the strong-coupling vacuum as the trial state, they agreed very well with them, improving confidence in the results.

The photon mass gap and the ratio  $R_g$  of the mass gap in the vacuum sector to the photon mass were also studied using a unistate and bistate contraction. The weak-coupling behavior of the photon mass differed from that of the Villain model but was in good agreement with the results of two previous calculations by other authors. Scaling in the mass ratio was observed for  $\beta > 2$  and the weak-coupling estimates of this ratio were consistent with a continuum limit value  $R_g = 2$ , providing no evidence of a stable scalar glueball. The bistate contraction was instrumental in enabling the accurate determination of both of the above quantities in the weak-coupling region. This suggests that use of the bistate contraction technique could lead to improved determinations of glueball and hadron masses in lattice QCD.

### 6.0.1 Acknowledgements:

I would like to thank Ted Barnes, Nathan Isgur, Jean Potvin, Eric Swanson, and Marvin Weinstein for helpful conversations. This work was supported by a grant from the Natural Sciences and Engineering Research Council of Canada and by the United States Department of Energy.

## TABLE CAPTIONS

- 1: Ground state energy density estimates compared to those of the guided random walk (GRW) algorithm on an  $8 \times 8$  lattice and strong- and weak-coupling perturbation theory (PT).
- 2: Comparison of mean plaquette  $\langle \cos \phi_p \rangle$  estimates. The results are compared to those obtained using the guided random walk (GRW) algorithm on an  $8 \times 8$  lattice and strong- and weak-coupling perturbation theory (PT).

## FIGURE CAPTIONS

- 1) All connected graphs consisting of up to six plaquettes which can be embedded on a square lattice. The circles represent plaquettes and the line segments connecting the circles represent the links of the lattice shared by adjacent plaquettes. The values in the upper right-hand corners are the strong embedding constants per site for the graphs in a square two-dimensional lattice.
- 2) Values of  $\lambda$  which minimize the expectation of the Hamiltonian in the state  $|\varphi_{\lambda\omega}\rangle$ .
- 3) The specific heat  $C^A$  in  $U(1)_{2+1}$  HLGT.
- 4) The lattice photon mass gap. The squares indicate the bistate contraction estimates  $M^B$  and the circles denote the  $M^A$  estimates. The dashed curve is the result from strong-coupling perturbation theory, while the solid curve is a straight line fit to the bistate estimates for  $1 \leq \beta \leq 2$  and the  $M^A$  estimates for  $1 \leq \beta \leq 1.4$ . The results of Hamer and Irving are shown as a dotted curve, and the dashed-dotted curve shows the results of Heys and Stump.
- 5) Ratio of the mass gap in the vacuum sector to the photon mass gap. The single state contraction estimates  $R_g^A$  are shown as circles, and the bistate contraction estimates  $R_g^B$  are displayed as squares. The solid curve is the result from strong-coupling perturbation theory.

- 6) Average bistate estimates of  $R_g$  for (a)  $\beta = 0.8$  and (b)  $\beta = 1.3$  as a function of  $i\omega$ . The parameter  $\omega$  is freely chosen and is imaginary;  $\lambda$  is then chosen so as to minimize the expectation value of the Hamiltonian in the state  $|\varphi_{\lambda\omega}\rangle$ .

## REFERENCES

1. Ken Wilson, *Phys. Rev. D* **10**, 2445 (1974).
2. John Kogut and Leonard Susskind, *Phys. Rev. D* **11**, 395 (1975).
3. A.M. Polyakov, *Phys. Lett.* **59B**, 82 (1975); *Nucl. Phys.* **B120**, 429 (1977).
4. T. Banks, R. Myerson, and J. Kogut, *Nucl. Phys.* **B129**, 493 (1977).
5. James Glimm and Arthur Jaffee, *Phys. Lett.* **66B**, 67 (1977).
6. Sidney D. Drell, Helen R. Quinn, Benjamin Svetitsky, and Marvin Weinstein, *Phys. Rev. D* **19**, 619 (1979).
7. Markus Göpfert and Gerhard Mack, *Comm. Math. Phys.* **82**, 545 (1982).
8. A., E., and P. Hasenfratz, *Nucl. Phys.* **B180** [FS2], 353 (1981).
9. J.B. Kogut, D.K. Sinclair, R.B. Pearson, J.L. Richardson, and J. Shigemitsu, *Phys. Rev. D* **23**, 2945 (1981).
10. V. Alessandrini, V. Hakim, and A. Krzywicki, *Nucl. Phys.* **B200** [FS4], 355 (1982).
11. A.C. Irving and C.J. Hamer, *Nucl. Phys.* **B235** [FS11], 358 (1984).
12. C.J. Hamer and A.C. Irving, *Z. Phys. C* **27**, 145 (1985).
13. Urs M. Heller, *Phys. Rev. D* **23**, 2357 (1981).
14. D. Horn and M. Weinstein, *Phys. Rev. D* **25**, 3331 (1982).
15. Thomas Hofsäss and Roger Horsley, *Phys. Lett.* **123B**, 65 (1983).
16. Peter Suranyi, *Phys. Lett.* **122B**, 279 (1983); *Nucl. Phys.* **B225** [FS9], 77 (1983).

17. W. Langguth, *Z. Phys. C* **23**, 289 (1984).
18. David W. Heys and Daniel R. Stump, *Nucl. Phys.* **B257** [FS14], 19 (1985).
19. David W. Heys and Daniel R. Stump, *Nucl. Phys.* **B285** [FS19], 13 (1987).
20. Peter Suranyi, *Nucl. Phys.* **B225** [FS9], 538 (1983).
21. Gernot Münster and Peter Weisz, *Nucl. Phys.* **B180** [FS2], 13 (1981).
22. A.C. Irving, J.F. Owens, and C.J. Hamer, *Phys. Rev. D* **28**, 2059 (1983).
23. G. Bhanot and M. Creutz, *Phys. Rev. D* **21**, 2892 (1980).
24. Eric D'Hoker, *Nucl. Phys.* **B180** [FS2], 341 (1981).
25. Jan Ambjorn, Anthony J.G. Hey, and Steve Otto, *Nucl. Phys.* **B210** [FS6], 347 (1982).
26. T. Sterling and J. Greensite, *Nucl. Phys.* **B220** [FS8], 327 (1983).
27. D. Dahl and R. Blankenbecler, *Phys. Rev. D* **32**, 977 (1985).
28. J. Potvin and T.A. DeGrand, *Phys. Rev. D* **30**, 1285 (1984).
29. T.A. DeGrand and J. Potvin, *Phys. Rev. D* **31**, 871 (1985).
30. David W. Heys and Daniel R. Stump, *Phys. Rev. D* **28**, 2067 (1983).
31. David Kotchan, Ph.D. thesis, "A Numerical Simulation of  $U(1)$  Gauge Theory on the Lattice," University of Toronto, 1990.
32. S.M. Eleutério and R.V. Mendes, CERN preprint TH.4181/85 (1985).
33. D. Horn and M. Weinstein, *Phys. Rev. D* **30**, 1256 (1984).
34. D. Horn, M. Karliner, and M. Weinstein, *Phys. Rev. D* **31**, 2589 (1985).
35. G.J. Mathews, N.J. Snyderman, and S.D. Bloom, *Phys. Rev. D* **36**, 2553 (1987).
36. D. Horn and E.G. Klepfish, Tel Aviv University Preprint 1791-90.
37. C.P. van den Doel and D. Horn, *Phys. Rev. D* **33**, 3011 (1986).

38. C.P. van den Doel, D. Horn, and A. Klatchko, *Phys. Lett.* **172B**, 399 (1986).
39. C.P. van den Doel and R. Roskies, *Phys. Rev. D* **34**, 3165 (1986).
40. C.P. van den Doel and D. Horn *Phys. Rev. D* **35**, 2824 (1987).
41. D. Horn and G. Lana, Tel Aviv University Preprint 1878-91.
42. D. Horn, G. Lana, and D. Schreiber, *Phys. Rev. D* **36**, 3218 (1987).
43. J.B. Kogut, *Rev. Mod. Phys.* **51**, 659 (1979).
44. S.E. Koonin, E.A. Umland, and M.R. Zirnbauer, *Phys. Rev. D* **33**, 1795 (1986).
45. C. Domb, *Adv. Phys.* **9**, 149 (1960).
46. G.S. Rushbrooke, *J. Math. Phys.* **5**, 1106 (1964).
47. M.F. Sykes, J.W. Essam, B.R. Heap, and B.J. Hiley, *J. Math. Phys.* **7**, 1557 (1966).

**Table 1:** Ground State Energy Density Estimates

$\beta$	$\epsilon_0^A$	$\epsilon_0^B$	GRW( $8 \times 8$ )	PT
0.25	0.246095(6)	0.2460951(1)	0.24610(1)	0.246095
0.50	0.46892(5)	0.46893(2)	0.46891(3)	0.46890
0.75	0.6471(1)	0.6474(2)	0.6467(1)	————
1.00	0.7675(4)	0.7689(9)	0.7676(7)	————
1.25	0.8344(3)	0.836(3)	0.8330(19)	————
1.50	0.8681(5)	0.869(3)	0.8726(31)	————
1.75	0.8860(5)	0.887(4)	0.8896(31)	————
2.00	0.898(1)	0.898(5)	0.8984(56)	0.9007
2.25	0.906(2)	0.905(5)	0.9165(63)	0.9071
2.50	0.912(1)	0.911(5)	————	0.9122
3.00	0.921(1)	0.919(4)	————	0.9198
4.00	0.931(3)	0.928(5)	————	0.9294

**Table 2: Mean Plaquette Estimates**

$\beta$	$\langle \cos \phi_p \rangle^A$	$\langle \cos \phi_p \rangle^B$	GRW( $8 \times 8$ )	PT
0.25	0.03124(4)	0.0313(2)	0.027(3)	0.03123
0.50	0.1238(2)	0.123(2)	0.121(2)	0.12381
0.75	0.2682(4)	0.267(3)	0.275(3)	——
1.00	0.4333(3)	0.437(3)	0.439(10)	——
1.25	0.5723(9)	0.575(2)	0.575(10)	——
1.50	0.663(3)	0.666(6)	0.664(15)	——
1.75	0.719(2)	0.722(10)	0.720(9)	——
2.00	0.757(4)	0.760(11)	0.777(12)	0.761
2.25	0.785(5)	0.788(13)	0.808(10)	0.787
2.50	0.807(5)	0.811(15)	——	0.808
3.00	0.840(5)	0.839(14)	——	0.840
4.00	0.881(3)	0.882(13)	——	0.880

Figure 1: Connected Diagrams

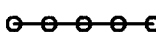
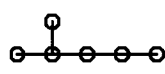
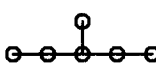
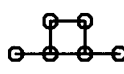
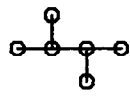
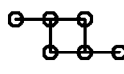
1  $G_1$	2  $G_2$	6  $G_3$	14  $G_4$
4  $G_5$	1  $G_6$	34  $G_7$	20  $G_8$
8  $G_9$	1  $G_{10}$	82  $G_{11}$	4  $G_{12}$
52  $G_{13}$	32  $G_{14}$	12  $G_{15}$	4  $G_{16}$
16  $G_{17}$	4  $G_{18}$	8  $G_{19}$	2  $G_{20}$

Figure 2

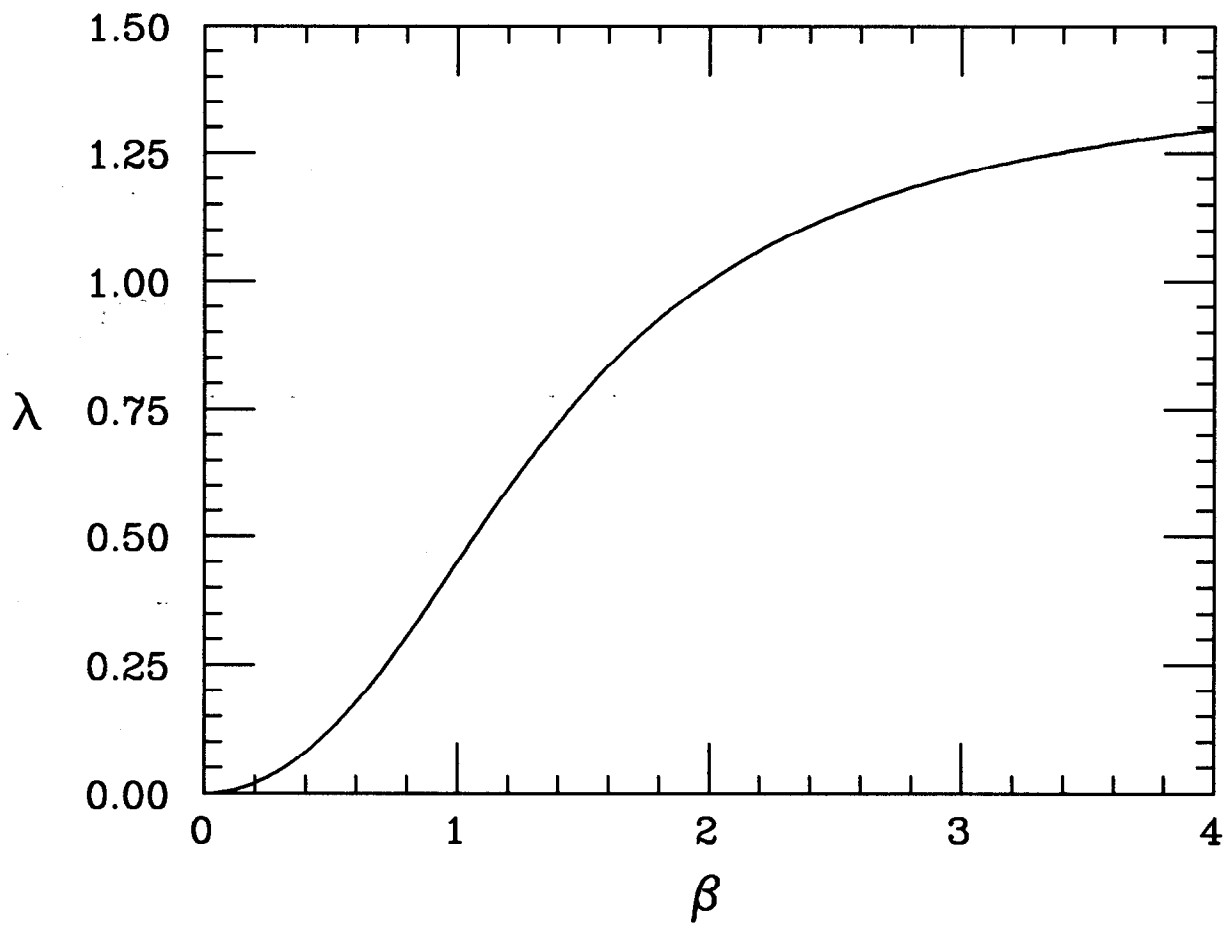


Figure 3: Specific Heat

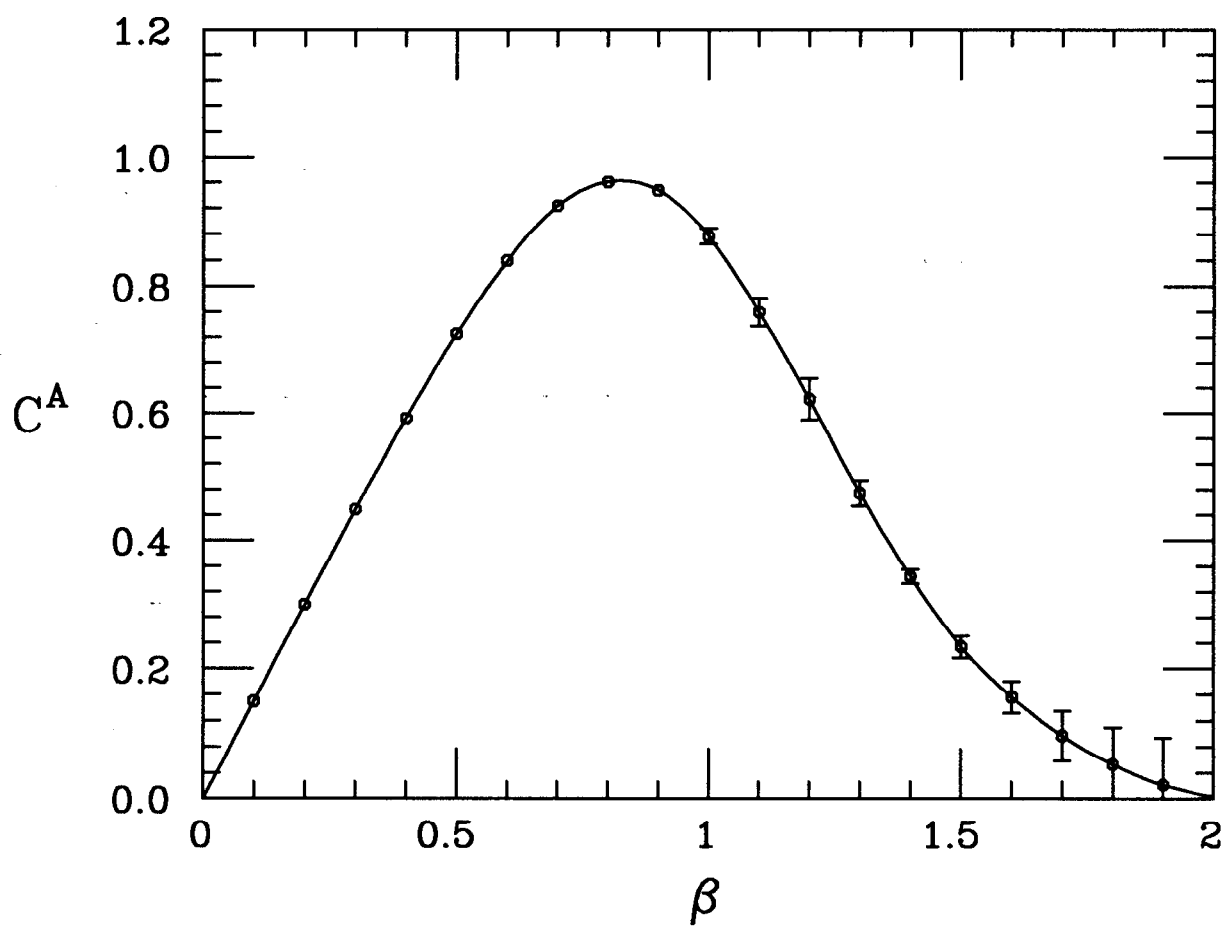


Figure 4: Photon Mass Gap

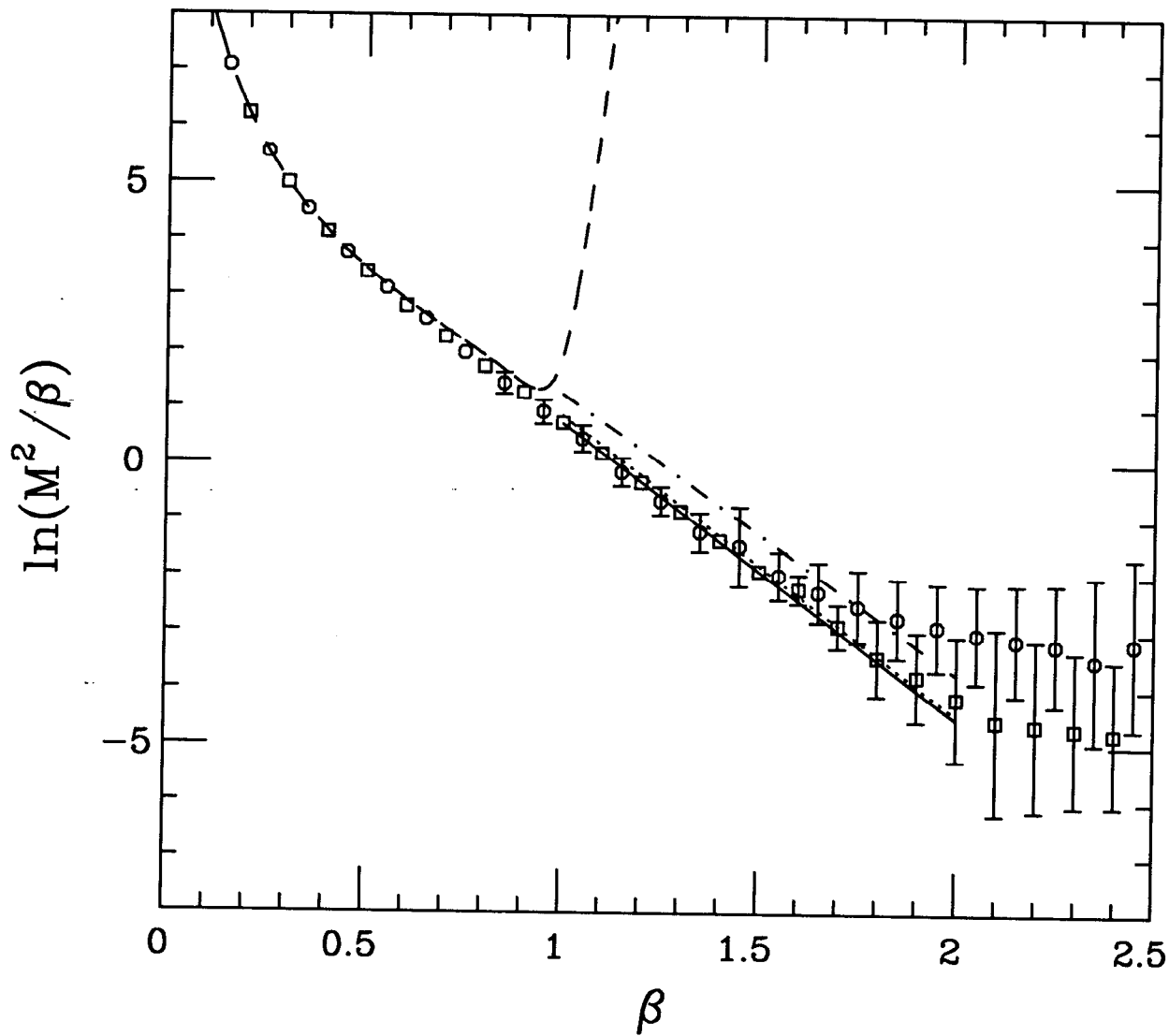


Figure 5: Mass Gap Ratio

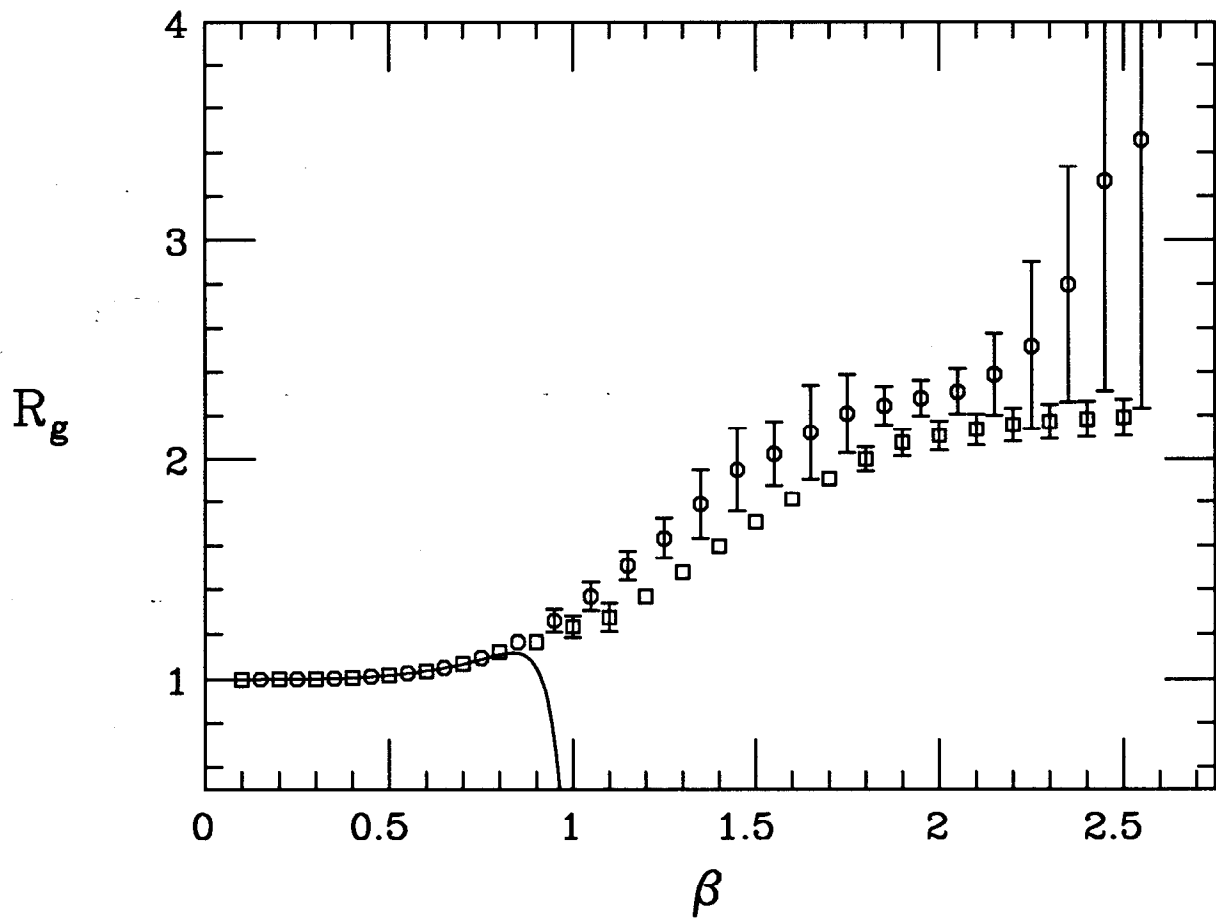


Figure 6(a):  $R_g^B$  ( $\beta=0.8$ )

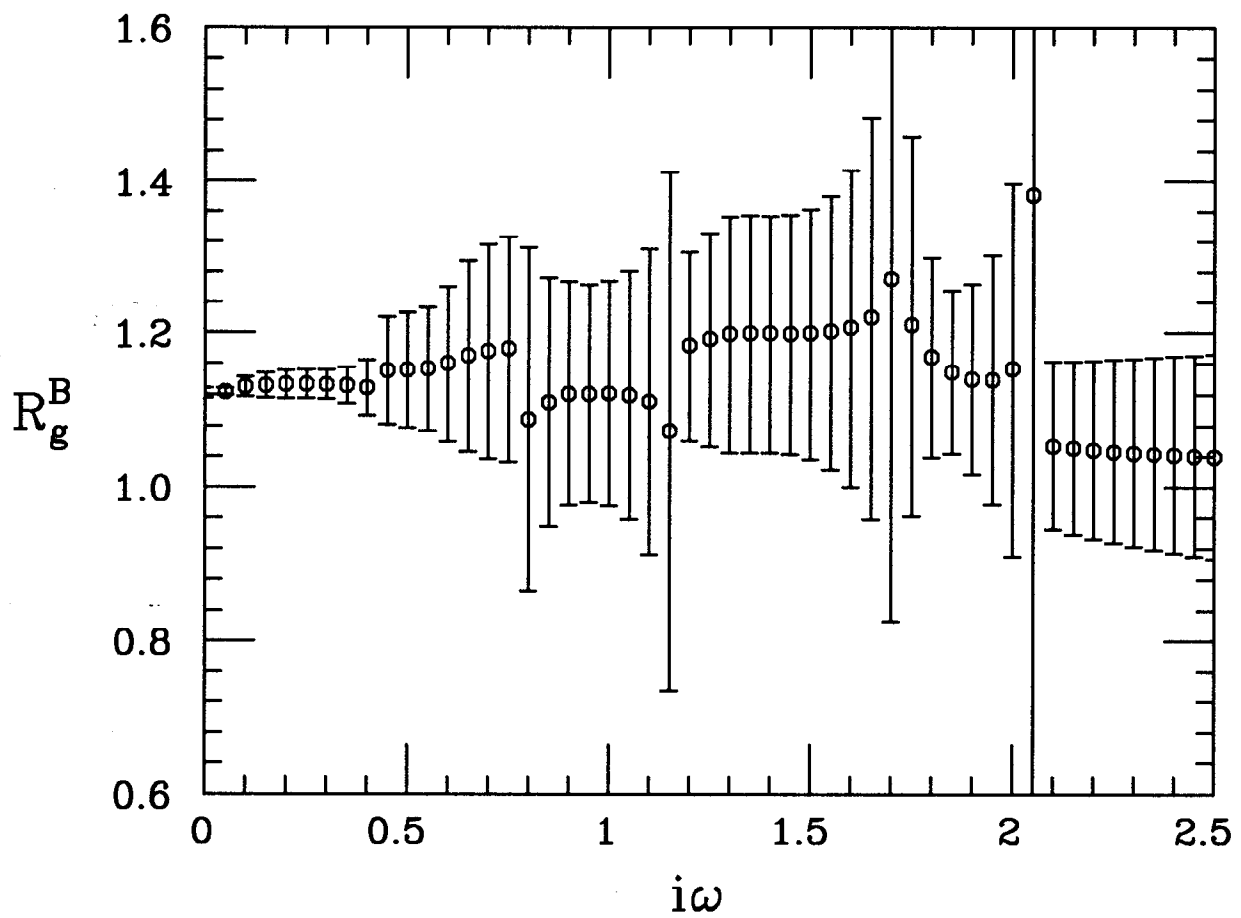


Figure 6(b):  $R_g^B$  ( $\beta=1.3$ )

